# Time-Resolved Ion Energy Measurements in the SPT-50 Hall Effect Thruster

Austen Thomas[1] and Kristina Lemmer[2]
*Western Michigan University, Kalamazoo, MI, 49008, USA*

Lee Johnson[3]
*Jet Propulsion Laboratory, California Institute of Technology, Pasadena, CA, 91109, USA*

**An investigation into time-resolved ion energy measurements of the 300-W SPT-50 Hall effect thruster (HET) utilizing a high-speed retarding potential analyzer (HSRPA) is presented. Ion energy as a function of HET operating condition and downstream position was measured. High-speed measurements were performed with a standard retarding potential analyzer (RPA) in conjunction with high-speed, low-noise circuitry, allowing fast collector current measurements at discrete retarding biases. Time-averaged and time-resolved ion energy measurements were observed to establish a relationship between ion energy, discharge conditions, and downstream position. Time-series data were reconstructed using data fusion techniques allowing time-resolved ion energy distribution functions (IEDFs) to be acquired. Time-resolved ion energy measurements varied in mean, peak-to-peak, and temporal characteristics as the operating conditions and position were varied.**

## I. Nomenclature

| | | |
|---|---|---|
| $A$ | = | Aperture area |
| $D$ | = | Embedding dimension |
| $E$ | = | Ion energy |
| $e$ | = | Elementary charge |
| $f$ | = | Distribution function |
| $I_{coll}$ | = | Collector current |
| $I_{max}$ | = | Maximum collector current |
| $k$ | = | Nearest neighbors |
| $m_i$ | = | Ion mass |
| $N$ | = | Sample depth |
| $n_i$ | = | Ion density |
| $T_e$ | = | Electron temperature |
| $V_{bias}$ | = | Retarding potential |
| $V_p$ | = | Plasma potential |
| $\tau$ | = | Time-lag |
| $\theta$ | = | Scattering angle |

## II. Introduction

Hall effect thrusters (HETs) have become a preferred method of electric propulsion (EP) for in-space applications, boasting an extensive flight heritage several decades long [1]. As EP thrusters rise in power, difficulty in testing these thrusters in ground-based facilities may reach limits such that data obtained during ground testing are no longer indicative of operation in-space. Therefore, predictive engineering models (PEMs) will be required to augment or

[1] Ph.D. Candidate, Mechanical and Aerospace Engineering, AIAA Student Member.
[2] Professor, Mechanical and Aerospace Engineering, AIAA Associate Fellow.
[3] Electric Propulsion Group, Senior Member AIAA.

potentially replace expensive and time-consuming ground testing. As new limits in power and propellant flow are reached, even testing in the largest vacuum facilities will encounter extreme facility effects. The result of these facility effects on thruster operation are not, at present, predicted by PEMs [2]. An alternative approach to understanding how to use PEMs to predict the operation of high-power EP systems is to operate lower power systems in a variety of vacuum facilities with differing pumping capacities and sizes. Data from these experiments can be extrapolated to higher powered systems in more capable vacuum facilities. Furthermore, the accessibility of low-power HETs allows research of new technologies and challenges facing HET development. In this work, a low-power HET will be used to aid in informing PEMs on the evolution of time-resolved ion energy.

Time-averaged plasma property measurements provide useful insight into the performance of HETs; however, as HETs exhibit dynamic behavior, time-resolved measurements are required to fully understand the operation of these devices. Several diagnostics exist to probe the plasma plume of an EP device to obtain temporal measurements, including high-speed dual Langmuir probes (HDLPs), time-resolved laser-induced fluorescence (TRLIF), and high-speed retarding potential analyzers (HSRPAs). These diagnostics provide insight into the origins of complex dynamic behavior, such as the breathing mode, spoke mode, axial transit time oscillations, and the electron drift instability, all of which can influence the performance and operation of HETs.

Among the various diagnostic techniques used to explore the dynamic behavior in an EP thruster plume, HSRPAs stand out due to their simplicity and effectiveness in providing valuable ion energy distribution data. A HSRPA is simply a standard retarding potential analyzer (RPA) used in connection with high-speed circuity. Other diagnostic tools such as E x B probes and laser-induced fluorescence (LIF) are capable of determining ion energy and velocity distributions but possess complex geometries and costly setups, respectively. As an alternative, RPAs can investigate issues regarding ion energy while possessing simple physical geometries and low cost. Recent developments utilizing an HSRPA have demonstrated the capability of producing time-resolved ion energy distribution functions (IEDFs) at various conditions [3–5]. These advancements enable RPAs to investigate plasma oscillations in HETs, further expanding their utility as a plasma diagnostic.

This investigation utilizes an HSRPA to study both spatial and temporal ion energy within the plume of a low-power HET. Time-resolved measurements provide critical insights into ion energy dynamics, shedding light on thruster instabilities. Such data are crucial in selecting the most effective operating conditions to balance thruster performance with longevity. Additionally, spatial measurements, particularly at large angles relative to the thruster centerline, are of significant interest due to the potential interactions between high-energy ions and spacecraft surfaces. To this end, this paper is organized as follows. First, the experimental setup is discussed in Section III, including the facility, test article, and diagnostics used to complete this work. Sections IV and V present the results obtained and a discussion of those results, respectively. Lastly, Section VI provides the final comments and conclusion of this investigation.

## III. Experimental Setup

### A. Facility

All testing was conducted at the NASA Jet Propulsion Laboratory (JPL) in the "Big Green" vacuum facility, a 2-m-diameter by 4.5-m-long cylindrical vacuum chamber, pictured in Fig. 1. The facility can achieve operational pressures ranging between $10^{-5}$ and $10^{-6}$ Torr through the use of three diffusion pumps and four cryogenic pumps. Background pressure was monitored by two Granville-Phillips Stabil-ion gauges located at the front and rear ends of the vacuum facility. Anode propellant flow rates were regulated by a Brooks Instrument GF series mass flow controller (MFC), while cathode flow was controlled by either a Brooks Instrument GF series or a Unit Instruments 8100 model MFC. Operating under diffusion pumps alone, the pressure was kept below $2.5 \times 10^{-5}$ Torr-Xe during thruster operation.

**Fig. 1 Big Green vacuum facility.**

### B. Test Article

Testing was conducted with the SPT-50, a 300-W HET with a 50 mm external diameter, developed by the Research Institute of Applied Mechanics and Electrodynamics of Moscow Aviation Institute [6, 7]. A heaterless 1.6 mm hollow cathode, supplied by Plasma Controls, LLC, was used as an externally mounted electron source for the SPT-50. Figure 2 shows the HET and cathode mounted in the vacuum facility in preparation for testing. For the presented work, the SPT-50 was operated at two conditions, 220-W (1.1 A, 200 V) and 330-W (1.1 A, 300 V), with the anode flow rate set to 12 sccm and the cathode flow rate set to 2.4 sccm. The thruster was mounted at the centerline of the vacuum facility and fired downstream toward the diagnostic setup, as illustrated in Fig. 3. To monitor the time-resolved telemetry of the thruster, a Textronix TCPA300 amplifier and TCP305 current probe were utilized. Those data were sampled by a Teledyne LeCroy HDO8038A 350 MHz oscilloscope. Time-averaged health monitoring of the thruster was performed by an OPTO-22 data acquisition system, including discharge properties, magnet currents, and cathode voltages.

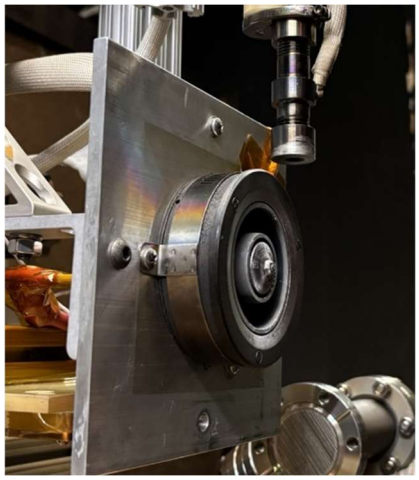

**Fig. 2 SPT-50 low-power HET.**

### C. Diagnostics

The diagnostics used in this investigation, including an HSRPA and an emissive probe, were placed on a 3-axis motion stage system downstream of the thruster, mounted on an 80/20 T-slotted frame, and fixed at thruster centerline height. At each spatial location, the diagnostics were aimed directly at the thruster centerline. Additionally, a

transimpedance amplifier (TIA) was mounted to the back of the RPA within the vacuum chamber, allowing line capacitance to be minimized between the RPA and TIA. Figure 3 illustrates the experimental setup utilized in this investigation, and Table 1 provides the exact diagnostic positions that were probed. The following sections describe the setup and functionality of each diagnostic tool.

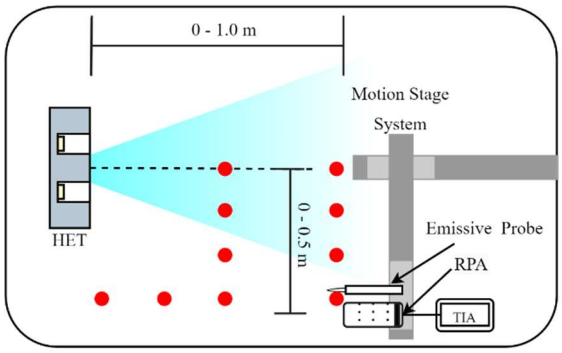


**Fig. 3 Experimental setup and diagnostic measurement locations.**

**Table 1 Measurement locations.**

| | Axial Distance | Radial Distance | Angle |
|---|---|---|---|
| **Position 0.1** | 70 mm | 487 mm | 82˚ |
| **Position 0.2** | 250 mm | 487 mm | 63˚ |
| **Position 1.1** | 500 mm | 487 mm | 44˚ |
| **Position 1.2** | 500 mm | 325 mm | 33˚ |
| **Position 1.3** | 500 mm | 163 mm | 18˚ |
| **Position 1.4** | 500 mm | 0 mm | 0˚ |
| **Position 2.1** | 1000 mm | 487 mm | 26˚ |
| **Position 2.2** | 1000 mm | 325 mm | 18˚ |
| **Position 2.3** | 1000 mm | 163 mm | 10˚ |
| **Position 2.4** | 1000 mm | 0 mm | 0˚ |

### i. Retarding Potential Analyzer

An RPA operates by establishing a variable electric field normal to incoming ions, creating a potential barrier that filters ions with energy lower than the sourced potential. The electric field within an RPA is formed by a series of mesh grids biased to various potentials. The RPA utilized in this study features a four-grid configuration, consisting of three electrostatically biased mesh grids and a floating grid, all in front of the current collection plate. The body, grids, retention rings, and wires are composed of 316 stainless steel. MACOR washers and a MACOR inner sleeve are used to insulate the grids from the RPA body and each other, while alumina tubing insulates the wires connected to the grids. Figure 4 shows a schematic of the RPA. Grid 1 is floating to minimize disturbance to the plasma from the biased grids. Grid 2 is negatively biased to repel plasma-born electrons from entering the RPA. Grid 3 is the retarding grid and is responsible for filtering ions. Grid 4 is biased negatively to suppress electron emission from the grids and collector due to the impact of high-energy ions. The RPA utilized in this investigation possesses an energy resolution, as determined by the geometry of the RPA grids, of approximately 1.5% of the retarding grid potential [8]. Further details on the construction of the RPA can be found in Ref. [5].

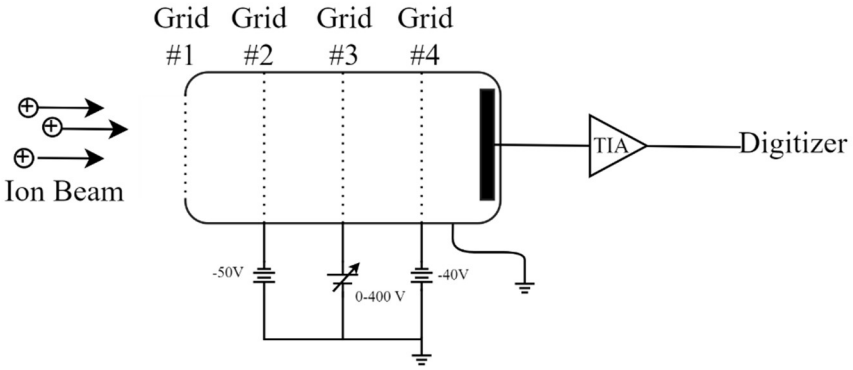


**Fig. 4 Retarding potential analyzer setup [4].**

Operationally, the retarding grid is swept over a range of positive potentials, filtering ions based on their energy per unit charge, *E/q*. Ions with an energy exceeding the retarding grid potential can pass and arrive at the collector, forming a measurable current. A relationship between the measured collector current and the sourced retarding grid potential can be established, forming an I-V trace. The negative first derivative of the collector current with respect to the retarding grid bias is directly proportional to the IEDF and is given by,

$$-\frac{dI_{coll}}{dV_{bias}} = Aen_i\sqrt{\frac{2E}{m_i}}f(E) \tag{1}$$

The IEDF is commonly approximated solely as the negative derivative of the collector current with respect to the retarding grid bias as it is the shape of the distribution function, rather than the magnitude, that is of concern.

$$f(E) \approx -\frac{dI_{coll}}{dV_{bias}} \tag{2}$$

The measurements collected in this investigation were performed at 150 discrete retarding grid potentials, with the retarding bias profile chosen to be $V_{bias}$ = [0:2:300] V for the 220-W condition and $V_{bias}$ = [0:3:196 198:2:350 355:5:400] V for the 330-W condition. This profile was selected to optimize the capture of discharge oscillations occurring near the thruster discharge voltage and obtain a sufficient energy resolution. A Keithley 237 source measurement unit was used to sweep the potential of the retarding grid, while the repelling and suppression grids were biased with a set of batteries to a potential of -50 V and -40 V, respectively. Collector current measurements were obtained using a FEMTO DHPCA-100 commercial TIA, a variable gain high-speed amplifier. Time-resolved RPA measurements were performed as follows: The retarding grid potential is held constant, as current is collected at a sample rate of 250 MS/s with the TIA. Simultaneously, a second measurement coupled to the HSRPA collector current measurement is sampled. In this investigation, the coupled measurement is the discharge current of the HET. The retarding grid potential is then increased by the appropriate voltage step size to obtain the desired IEDF resolution. This process is then repeated until a complete distribution is achieved.

Time-series data reconstruction was achieved through a data fusion technique known as shadow manifold interpolation (SMI), a non-linear technique based on manifold reconstruction and convergent cross-mapping (CMM) from Takens and Sugihara, respectively [9, 10]. In this investigation, the SMI parameters were held constant, for a given SPT-50 operating condition, to maintain consistency between reconstructions. The SMI parameters used are listed in Table 2.

**Table 2 SMI Parameters**

| Parameter | 200 V, 1.1 A | 300V, 1.1 A |
|---|---|---|
| ***D*** | 20 | 15 |
| ***τ (Sa)*** | 4 | 2 |
| ***k*** | 100 | 100 |
| ***N (Sa)*** | 15,000 | 15,000 |

Details on SMI and its parameters can be found in Refs [3, 4, 11]. The reconstructed waveforms are then assembled to form I-V curves at each representative point in time. Subsequently, signal noise was reduced by applying a Savitzky–Golay filter to the data after reconstruction and a smoothing spline to the reconstructed I-V curves. Time-resolved IEDFs were determined using Equation (2).

## ii. Emissive Probe

To facilitate time-averaged and time-resolved plasma potential measurements, a floating emissive probe was utilized. The floating emissive probe with the large emission method was selected for its simplicity and ability to provide temporal data. The measurement method and probe construction followed the recommended practices by Sheehan, *et al.* [12, 13]. The emissive probe used in this investigation is depicted in Fig. 5. Bored alumina tubing was used as the housing and isolating material. Bare strand 18 AWG copper wire was inserted along the full length of the bored holes of the alumina tube. A 0.1-mm-diameter tungsten wire was inserted into the copper strands in a hairpin configuration, extending 2-3 mm outward. To isolate the copper wire from the plasma, Ceramabond was applied over the surface of the alumina tube. The emissive probe was located approximately 25 mm from the orifice of the RPA.

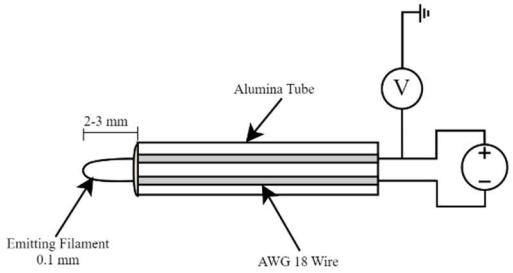


**Fig. 5 Emissive probe setup.**

Plasma potential measurements are required as the retarding grid of the RPA is ground-referenced. Therefore, the true ion energy from the RPA is calculated using Equation (3).

$$E = eV_{bias} - eV_p \tag{3}$$

The plasma potential can be identified by determining where the floating potential of the emissive probe saturates. As the emission current increases, the floating potential of the emissive probe approaches the plasma potential. Starting from a state of no emission, the floating potential rises rapidly toward the plasma potential due to a drop in the sheath potential of the probe. The change in floating potential eventually plateaus near the plasma potential and increasing the emission current further results in only a small increase in the floating potential due to space charge effects [12]. Figure 6 illustrates this behavior through the I-V characteristics obtained in this work. The plasma potential can be identified by using the method proposed by Kemp and Sellen, where the intersection of linearly fitted lines in the rapidly growing region and the saturation region estimates the plasma potential [14].

Time-resolved plasma potential measurements are conducted by heating the filament such that the emission current is in excess of the electron saturation current and sampling at a rate to capture the desired dynamics. This occurs at a floating potential past the time-averaged plasma potential. Measurements must be made deep enough into the electron saturation regime to ensure the accurate capture of the oscillation waveform, without going below the DC plasma potential. To obtain an accurate picture of both time-averaged and time-resolved plasma potential, the peak-to-peak

plasma potential oscillations are superimposed over the time-averaged plasma potential measurement. In this work, the high-speed plasma potential measurements were sampled at 250 MS/s.

## IV. Results

### A. Time-Averaged Measurements

Time-averaged ion energy and plasma potential were determined by averaging HSRPA measurements and performing slowly sampled floating emissive probe measurements. Figure 6 displays I-V characteristics obtained from the emissive probe at both the 220-W condition (Fig. 6a) and the 330-W condition (Fig. 6b) at the various positions described in Table 1, with the plasma potential denoted by the red marker on each I-V trace. Spatial variation in the plasma potential was observed, with the greatest potentials occurring near the thruster centerline. At 220-W, the plasma potential ranged from 4.6 V at position 0.1 to 7.7 V at position 1.4, whereas for the 330-W operating condition, the plasma potential ranged from 4.9 V – 8.2 V, with the maximum and minimum occurring at the same respective positions as the 220-W operating condition. A summary of the time-averaged data measured at each location is provided in Table 3. The plasma potential measurements will be used to correct the ion energy measured by the RPA for local plasma potential, as indicated in Equation (3).

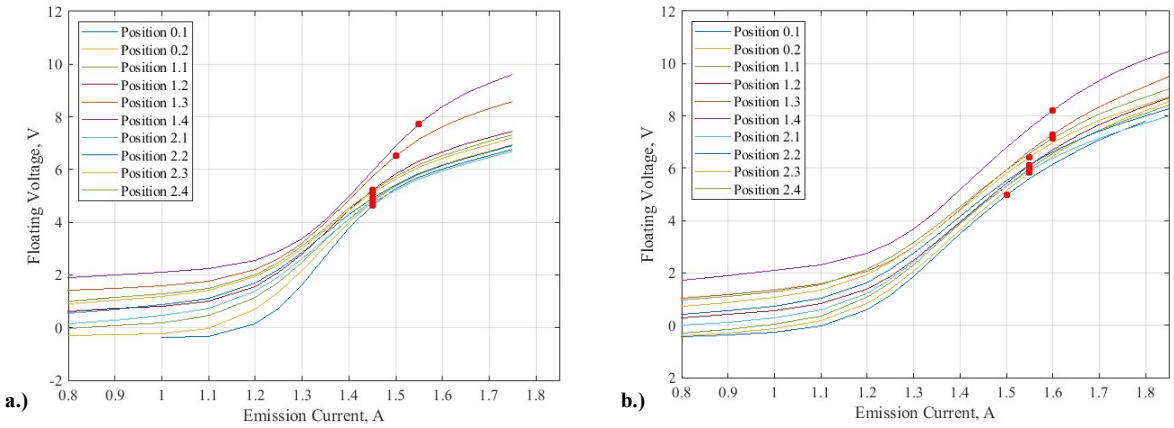


**Fig. 6 Time-averaged plasma potential measurements a.) 220-W (200 V, 1.1A) and b.) 330-W (300 V, 1.1A).**

Figure 7 shows the time-averaged I-V curves obtained from the RPA and the corresponding IEDFs at the 220-W operating condition for all positions. In the figure, the axial distance increases from 70 mm in Fig. 7a to 250 mm in Fig. 7b, while Figs. 7c through 7f are taken at 500 mm with decreasing transverse distances. Similarly, Figs. 7g through 7j correspond to an axial distance of 1000 mm, again with decreasing transverse distances. All I-V curves and IEDFs are normalized to their maximum measured value. At the high centerline angle positions (Fig. 7a – 7c, and 7g), the IEDFs display a prominent low-energy population. In fact, this low-energy population is the most probable population of the IEDF at positions 0.1 and 0.2. In this region of the plume, between 44° and 82° from the centerline, the lower energy ion populations measured are charge exchange (CEX) ions and elastically scattered ions.

It is typical for CEX ions to possess energies existing in the 0 eV – 50 eV range while elastically scattered ions would be expected to be between 50 eV – 150 eV, at the 200 V discharge condition [15]. Another notable feature in Fig. 7a – 7c is a minor peak centered between 125 eV and 175 eV, which grows in magnitude as the axial position within the plume increases, coinciding with a reduction in angle from centerline. The increase in the probability of this peak is a result of a greater number of primary ion beam ions being detected. The features observed in Fig. 7a – 7c, are further reflected by their respective I-V curves, showing a rapid decline in measured collector current at lower retarding grid potentials.

Measurements near the centerline (Fig. 7e, 7f, 7i, and 7j), show a distinct peak in each time-averaged IEDF, centered around the expected ion energy equivalent to the acceleration potential of 168 eV – 178 eV. As indicated by the corresponding I-V curves, the majority of ion current is effectively filtered out at the most probable ion energy. Additionally, it is the centerline positions that possess the narrowest distributions, with full-width half maximums (FWHMs) of 32 eV. As the centerline angle is decreased toward 0˚, fewer CEX and elastically scattered ions are

measured, reducing the width of the IEDF. At the intermediate positions 1.2 and 2.2 (Fig. 7d and Fig. 7h), a significant presence of the primary beam ions is observed, in addition to a moderate population of what are likely elastically scattered ions in the 50 eV – 150 eV range. Table 3 summarizes all time-averaged data obtained in this work, including plasma potential, most probable ion energy, and the FWHMs of the IEDFs.

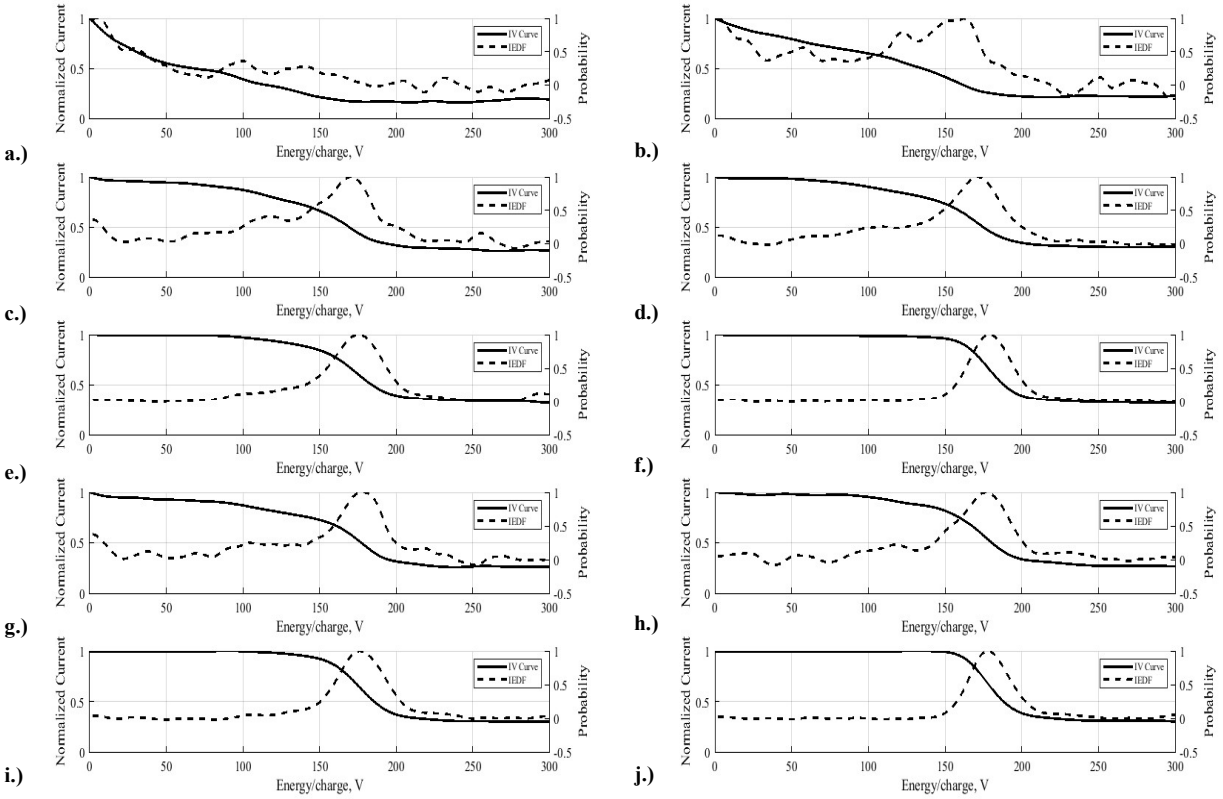


**Fig. 7 Time-averaged normalized I-V curves ($I_{coll}/I_{max}$) and IEDFs at a.) Position 0.1, b.) Position 0.2, c.) Position 1.1, d.) Position 1.2, e.) Position 1.3, f.) Position 1.4, g.) Position 2.1, h.) Position 2.2, i.) Position 2.3, and j.) Position 2.4 at 220-W (200 V, 1.1 A).**

Figure 8 presents the time-averaged I-V curves and IEDFs for the 330-W operating condition, displaying similar features to those in Fig. 7. As with the previous condition, measurements closer to the centerline (Fig. 8d – 8f and Fig. 8h – 8i) show a greater presence of primary beam ions, while more elastically scattered and CEX ions are measured at positions further off-centerline (Fig. 8a – 8c). Figure 8a – 8c, primarily shows populations of CEX and elastically scattered ions, with a minor contribution from the primary ion beam, measured around 200 eV – 260 eV. At positions 1.1 through 2.4 (excluding position 2.1), where the centerline angle is between 0 – 44°, the most probable ion energy corresponds to the primary ion beam, measured between 248 eV – 254 eV. The FWHM of the primary ion beam populations at the near centerline positions (0 – 44°), increased with increasing distance from the centerline, with the narrowest distributions occurring at the centerline positions 1.4 and 2.4, with widths of 60 eV and 54 eV, respectively. All time-averaged measurements from the 330-W operating condition are displayed on the right side of Table 3. It is important to note, an error occurred during the measurement at position 2.1, resulting in an unusable I-V curve and IEDF. The cause of this error is unknown; therefore, this data set is excluded.

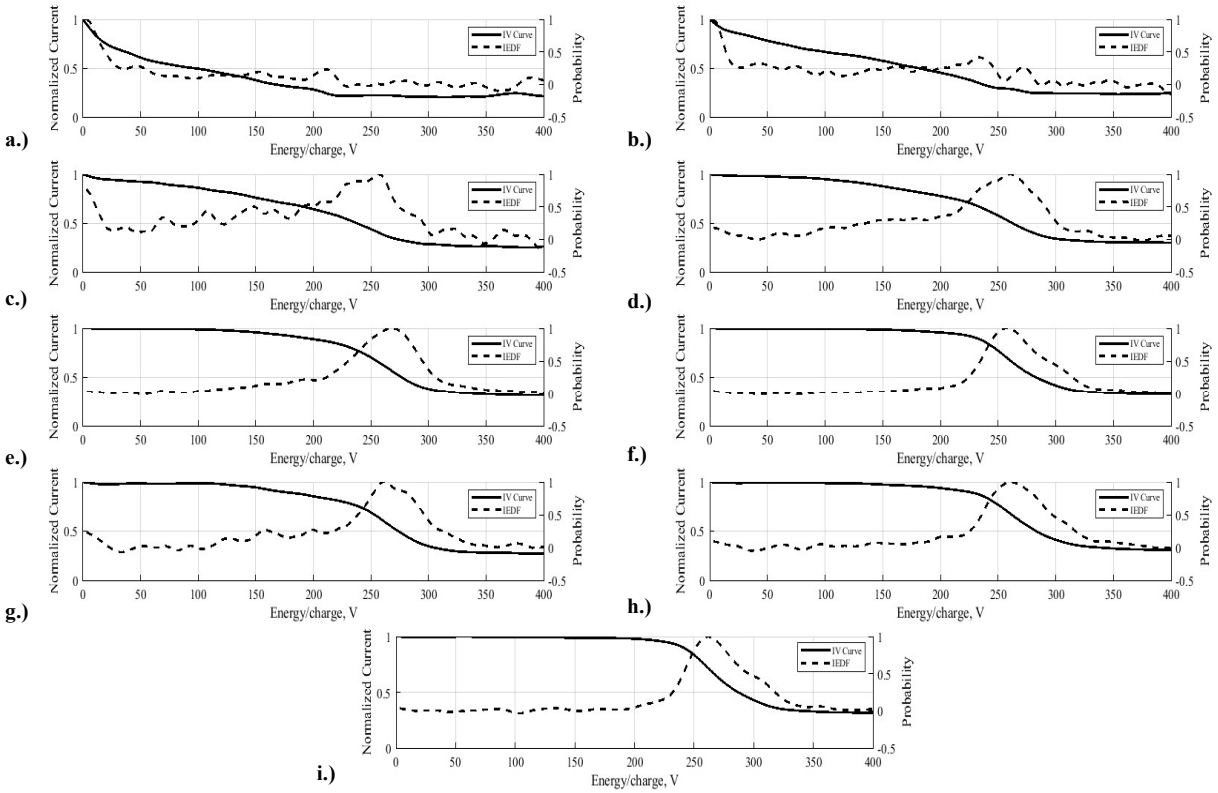


**Fig. 8 Time-averaged normalized I-V curves ($I_{coll}/I_{max}$) and IEDFs at a.) Position 0.1, b.) Position 0.2, c.) Position 1. 1, d.) Position 1.2, e.) Position 1.3, f.) Position 1.4, g.) Position 2.2, h.) Position 2.3, and i.) Position 2.4 at 330-W (300 V, 1.1 A).**

**Table 3 Time-Averaged Data**

| | 200 V 1.1 A | | | 300 V 1.1 A | | |
|---|---|---|---|---|---|---|
| | **$V_P$** | **Most Probable Ion Energy** | **FWHM** | **$V_P$** | **Most Probable Ion Energy** | **FWHM** |
| **Position 0.1** | 4.6 V | 2 eV | 32 eV | 4.9 V | 2 eV | 18 eV |
| **Position 0.2** | 4.7 V | 159 eV | 26 eV | 5.8 V | 2 eV | 15 eV |
| **Position 1.1** | 4.8 V | 163 eV | 42 eV | 5.9 V | 248 eV | 86 eV |
| **Position 1.2** | 5.2 V | 165 eV | 42 eV | 6.1 V | 252 eV | 70 eV |
| **Position 1.3** | 6.5 V | 168 eV | 40 eV | 7.3 V | 259 eV | 62 eV |
| **Position 1.4** | 7.7 V | 170 eV | 32 eV | 8.2 V | 250 eV | 60 eV |
| **Position 2.1** | 4.7 V | 171 eV | 36 eV | 5.9 V | NA | NA |
| **Position 2.2** | 4.9 V | 169 eV | 40 eV | 6.1 V | 254 eV | 58 eV |
| **Position 2.3** | 5.1 V | 169 eV | 38 eV | 6.4 V | 254 eV | 60 eV |
| **Position 2.4** | 5.2 V | 171 eV | 32 eV | 7.1 V | 253 eV | 54 eV |

## B. Time-Resolved Measurements

Time-resolved measurements conducted in this investigation have provided insight into the evolving plasma dynamics within the plume of low-power HETs. High-speed emissive probe measurements were conducted to estimate plasma potential fluctuations and correct the variation in peak-to-peak ion energy. An example of such a measurement recorded in this work is shown in Fig. 9, where the time-resolved emissive probe trace is displayed with the discharge current measurement. An approximation for peak-to-peak plasma potential oscillations is obtained by calculating the maximum peak-to-peak amplitude of the plasma potential over a period of roughly five breathing mode cycles.

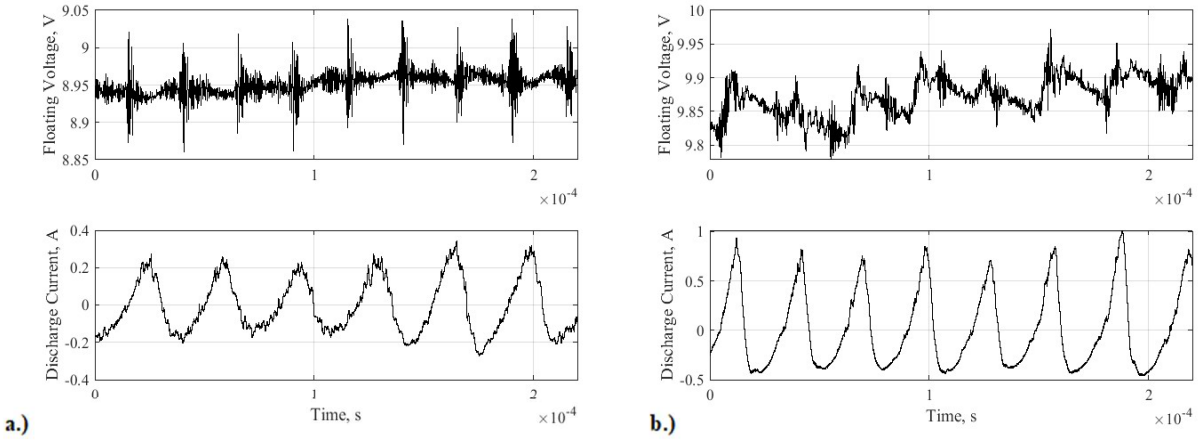


**Fig. 9 Time-resolved (top) emissive probe floating voltage position 1.4 and (bottom) AC discharge current a.) 220-W (200 V 1.1A) and b.) 330-W (300 V 1.1A).**

As illustrated by Fig. 9, the plasma potential oscillates at the breathing mode frequency of approximately 27.8 kHz at the 220-W condition and 32.5 kHz for the 330-W condition, consistent with expectations. The maximum variation in the peak-to-peak amplitude of the plasma potential ranged between 0.04 V – 0.2 V across all positions. Since these values fall well below the energy resolution of the RPA (1.5% of $V_{bias}$), the applicable correction is negligible. As such, no corrections are applied to the peak-to-peak ion energy measurements.

Time-resolved IEDFs at all measurement locations are displayed in Fig. 10 for the 220-W operating condition. At the 220-W operating condition, the primary ion beam population oscillates at the breathing mode frequency of 27.8 kHz, most notably in Fig. 10e – 10j. Figure 10c –10j display IEDFs with the most probable ion energy population centered around the expected acceleration potential, possessing a mean most probable ion energy ranging from 162 eV – 174 eV, with peak-to-peak ion energy oscillations between 18 eV – 76 eV. It should be noted, that the peak-to-peak ion energy references the range of the most probable energies. The mean most probable ion energy calculated from the data reconstruction is in relatively good agreement with the time-averaged calculated by directly averaging the HSRPA data. Minor discrepancies are due to data reconstruction variations. Two additional ion energy populations centered around the primary ion beam population can be observed in Fig. 10c – 10j, appearing with a moderate probability of ~0.5. These additional populations oscillate with the primary ion beam population at approximately ± 25 eV of the DC acceleration potential. One population lies just below the primary ion beam population between 150 eV – 175 eV and the other lies just above it between 185 eV – 200 eV. These moderate probability populations span an energy spectrum comparable to the FWHM of the time-averaged IEDFs. These populations are likely the result of the oscillatory nature of the discharge, resulting in ions being accelerated over varying potential drops near the DC acceleration potential.

Two lower-energy populations can be easily identified in the IEDFs at positions 0.1 and 0.2 (Fig. 10a and Fig. 10b) with partial visibility at positions 1.1 and 2.1 (Fig. 10c and Fig. 10g). The first population is observed in the 50 eV – 150 eV range, and the second population is in the 0 eV – 50 eV range. The 50 eV – 150 eV energy population likely arises from ions being born at lower electric potentials or suffering momentum loss due to elastic collisions. The second lower-energy population in the 0 eV – 50 eV range, is believed to be a CEX ion population. Literature shows that this population is most prominent near the plume edge, vacuum chamber walls and in the background plasma behind the thruster, as this area is dominated by CEX ions [15–17]. The CEX ions are most prominent when the RPA was placed in the high centerline angle side plume regions at positions 0.1 and 0.2 as depicted in Fig. 10a and Fig. 10b. The CEX ion population also oscillates at the breathing mode frequency, 27.8 kHz. The production of CEX ions is closely coupled to the discharge of the HET; therefore, the CEX ion populations exhibit characteristics of the discharge, such as fluctuating at the breathing mode frequency [17]. Table 4 summarizes the primary features of each time-resolved IEDF.

The time-resolved IEDFs measured at the 330-W condition are shown in Fig. 11, exhibiting features similar to those observed at the 220-W condition. The primary ion beam population oscillates at the breathing mode frequency

of 32.5 kHz, centered around the acceleration potential, and ranges between 253 eV – 270 eV. These oscillations, driven by the breathing mode, possess peak-to-peak ion energy amplitudes between 44 eV – 86 eV. As was observed at the 220-W condition, two moderate probability populations oscillate with the primary ion beam population within ± 50 eV of the acceleration potential. This population is again thought to result from ions experiencing various acceleration potentials. The lower of the two populations exists in the 225 eV – 265 eV range, while the higher energy population ranges from 275 eV – 335 eV.

A notable feature not observed at the 220-W condition was found in the time-resolved IEDFs at the 330-W condition, particularly as measurements were made closer to the centerline. At high centerline angles (positions 0.1 and 0.2), similar CEX and elastically scattered populations were observed at both conditions, with equivalent probabilities. However, as measurements were conducted closer to the centerline of the plume at the 330-W condition, where the probability of detecting primary beam ions increases, a branching feature emerged, extending between the CEX population and the primary ion beam population. This feature is most apparent at position 1.1 (Fig. 11c), where it peaks and ranges between 75 eV – 200 eV. As the plume is probed closer toward the centerline this feature fades, but some artifacts remain in the IEDF. At an axial distance of 1 m, this branching effect remains partially visible up to position 2.3. This feature is further discussed in Section IV and briefly in the following paragraph. Additionally, as was noted with the time-averaged measurements, an error occurred at position 2.1.

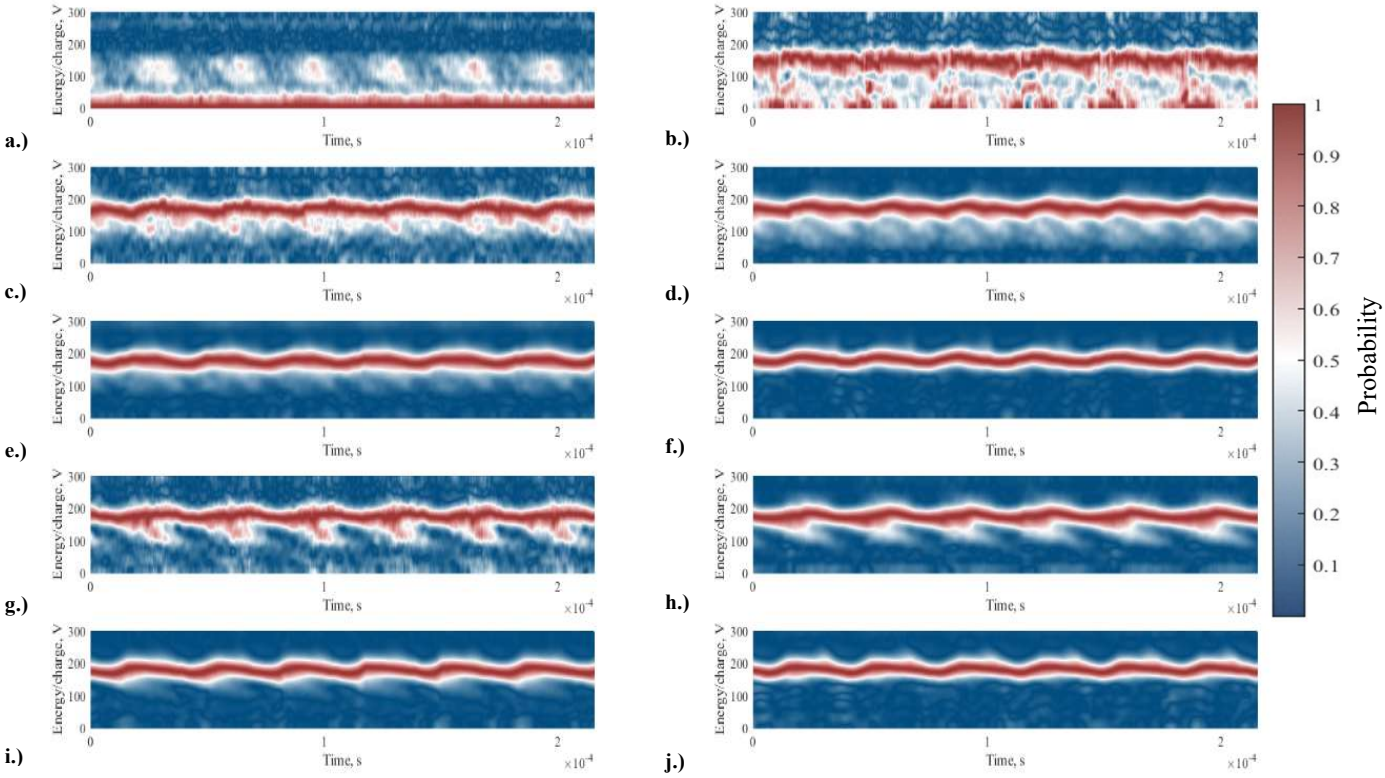


**Fig. 10 SPT-50 time-resolved IEDFs at 220-W operating condition (200 V, 1.1 A) at a.) Position 0.1, b.) Position 0.2, c.) Position 1.1, d.) Position 1.2, e.) Position 1.3, f.) Position 1.4, g.) Position 2.1, h.) Position 2.2, i.) Position 2.3, and j.) Position 2.4.**

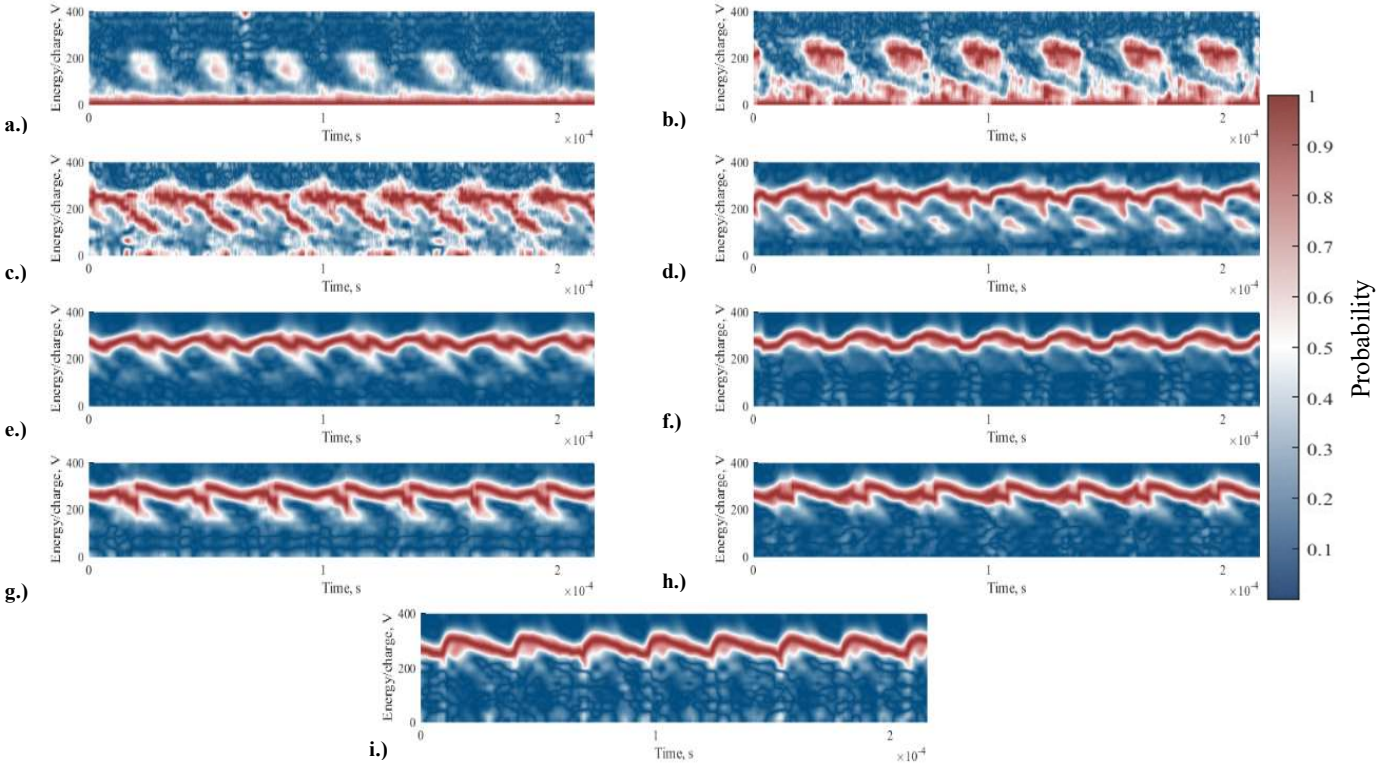


**Fig. 11 SPT-50 time-resolved IEDFs at 330-W operating condition (300 V, 1.1 A) at a.) Position 0.1, b.) Position 0.2, c.) Position 1.1, d.) Position 1.2, e.) Position 1.3, f.) Position 1.4, g.) Position 2.2, h.) Position 2.3, and i.) Position 2.4.**

**Table 4 Time-Resolved Data SPT-50.**

| | 200 V 1.1 A | | | 300 V 1.1 A | | |
|---|---|---|---|---|---|---|
| | **Mean Most Probable Ion Energy** | **Peak-to-Peak Amplitude** | **Frequency** | **Mean Most Probable Ion Energy** | **Peak-to-Peak Amplitude** | **Frequency** |
| **Position 0.1** | 2 eV | 108 eV | 27.8 kHz | 1 eV | 27 eV | 32.5 kHz |
| **Position 0.2** | 140 eV | 168 eV | 27.8 kHz | 196 eV | 232 eV | 32.5 kHz |
| **Position 1.1** | 162 eV | 76 eV | 27.8 kHz | 210 eV | 272 eV | 32.5 kHz |
| **Position 1.2** | 164 eV | 20 eV | 27.8 kHz | 253 eV | 86 eV | 32.5 kHz |
| **Position 1.3** | 168 eV | 20 eV | 27.8 kHz | 260 Ev | 44 eV | 32.5 kHz |
| **Position 1.4** | 172 eV | 18 eV | 27.8 kHz | 268 eV | 56 eV | 32.5 kHz |
| **Position 2.1** | 171 eV | 68 eV | 27.8 kHz | NA | NA | NA |
| **Position 2.2** | 171 eV | 34 eV | 27.8 kHz | 259 eV | 78 eV | 32.5 kHz |
| **Position 2.3** | 173 eV | 22 eV | 27.8 kHz | 264 eV | 50 eV | 32.5 kHz |
| **Position 2.4** | 174 eV | 22 eV | 27.8 kHz | 270 eV | 52 eV | 32.5 kHz |

Figure 12 displays the time-aligned IEDFs plotted alongside discharge current for positions 1.1 and 1.4 at the 220-W condition. To achieve this a time delay is applied to the time-resolved IEDF based upon the energy of the ions and the expected time of flight to the RPA. These time-aligned plots allow for a direct comparison between ion generation and specific moments in the discharge current waveform, quantifying their relationship. Notably, the trough of the IEDF approximately corresponds with the peak of the discharge current, while the peak of the IEDF aligns with the rising phase of the discharge current. This indicates that peak ion energies occur at the time of increasing ionization, while lower energies are observed at maximum ionization. This is expected, given that the discharge current and

voltage exhibit a 90° phase shift. In comparing Fig. 12a and Fig. 12b, the IEDF at position 1.1 shows more distortion, but both retain similar temporal characteristics of the breathing mode. The IEDF of Fig. 12a presents a broader distribution than that observed at position 1.4 in Fig. 12b, with the most probable peak-to-peak ion energy spanning from 125 eV – 200 eV, compared to the 160 eV – 200 eV of Fig. 12b. This behavior is consistent with detecting additional ion energy populations, specifically, primary and elastically scattered ions. As expected, these lower-energy populations near 125 eV occur near the troughs of the discharge current. Figure 13 shows the IEDFs at the 330-W condition at the same positions as Fig. 12, with a notable feature not present at the 220-W condition. This feature is a branching structure, extending from primary ion beam energies to lower elastically scattered energies. At position 1.1, the branching feature exists between the minimum discharge current and approximately 25% of the peak discharge current. While the comparison between the time-resolved IEDF and discharge current establishes a relationship between ion energy and generation, it cannot inform upon ion energy in the plume due to collisional scattering.

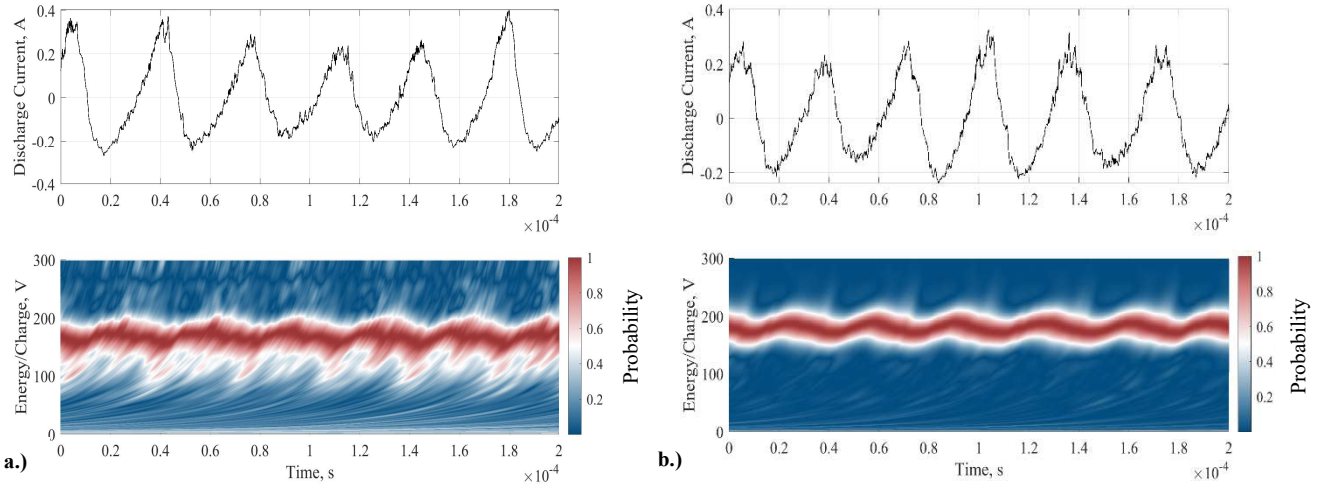


**Fig. 12 SPT-50 AC discharge current (top) and time-aligned time-resolved IEDF at 220-W operating condition (200 V, 1.1 A) (bottom) a.) position 1.1 and b.) position 1.4.**

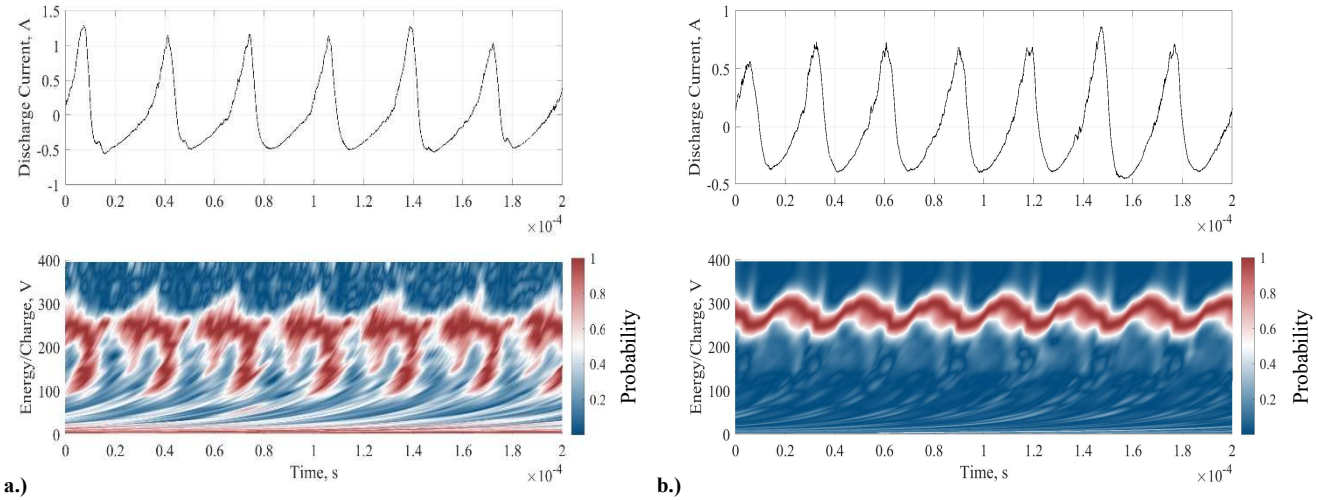


**Fig. 13 SPT-50 AC discharge current (top) and time-aligned time-resolved IEDF at 330-W operating condition (300 V, 1.1 A) (bottom) a.) position 1.1 and b.) position 1.4.**

## V. Discussion

The preceding section presented spatial measurements of time-averaged and time-resolved ion energy and plasma potential within the plume of an SPT-50 HET operating on xenon at 220-W and 330-W. The measurements showed

variations of ion energy both spatially and across different operating conditions, resulting in the measurement of several ion energy populations.

### A. Time-Averaged Measurements

Time-averaged data were collected to provide a reference for comparison to time-resolved data. In examining the time-averaged emissive probe data, the spatial variation of plasma potential followed expected trends. The plasma potential ranged between 4.6 V – 8.2 V across all positions for both operating conditions, with the maximum measured values occurring at centerline locations and the minimum at the greatest transverse distance. In regions where the density and electron temperature are expected to be lower, such as those far downstream of the thruster channel exit or at high-centerline angles, lower plasma potentials were measured [15]. The floating emissive probe method possesses an uncertainty in the measurement of the floating potential of $0.1T_e/e$ [18]. At the measurement locations performed in this work $T_e$ is typically on the order of $\sim 1$ eV, resulting in a relatively small error [19]. In a previous investigation involving another sub-kilowatt HET, the SPT-70, operated at approximately 675-W (300 V, 2.25 A), spatial plasma potential measurements were performed by Kim *et al.* utilizing emissive and Langmuir probes, 0.5 m from the channel exit at several azimuthal locations [20]. Kim recorded plasma potential measurements ranging from 25 V – 30 V across all azimuthal positions, with the lowest potentials at the greatest centerline angles. While the thruster operating power was over 2.5 times greater than that observed in the current experiment, insight can still be drawn regarding the magnitude of potential variation across azimuthal locations, which displayed results similar to the investigation performed here.

Time-averaged ion energy measurements also demonstrated the expected trends with increasing discharge voltage and spatial variation, namely the measurement of different ion energy populations. At both operating conditions, as the discharge voltage was increased, the most probable ion energy increased in proportion. Additionally, the FWHM narrowed as the measurements were made closer to the centerline, resulting from ions being born at a smaller range of acceleration potentials. As different locations within the plume were probed, various ion energy populations detected, ranging from primary beam ions near the centerline to elastically scattered and CEX ions at moderate to high centerline angles (45 – 90°). As shown in Fig. 7a for the 220-W condition and Fig. 8a for the 330-W condition, a greater probability of measuring CEX ions is found at high centerline angles. This CEX population remains prominent in the IEDF until the centerline angle decreases to under 45°. These CEX collisions result in large-angle scattering of 90° or higher; thus, greater quantities of CEX ions are measured at locations where the centerline angle was high, such as positions 0.1 – 1.1 [15, 21, 22].

At intermediate centerline angles, ions possessing energies in the 50 eV – 150 eV range for the 220-W condition or 50 eV – 225 eV range for the 330-W condition were observed primarily in the IEDFs of Fig. 5 and Fig. 6, plots a – d. Ions in this energy range are indicative of populations that have experienced energy loss due to elastic collisions. At the measurement locations within the plume with centerline angles between 33° – 66°, the energy of an ion that undergoes an ideal elastic collision and is scattered at an angle $\theta$ by another ion initially at rest is proportional to $Ecos^2(\theta)$ [15]. Assuming the ion beam possesses an energy of around 175 eV or 270 eV and is scattered at 33° – 66°, the expected range of energies is between 30 eV – 125 eV and 45 eV – 190 eV, respectively. The energies observed Fig. 7 and Fig. 8 fall within these ranges. The last population observed in the time-averaged IEDFs is the primary ion beam population. The primary ion beam is most prominent at measurement locations where the centerline angle is small (< 45°), forming a distinctive peak near the acceleration potential.

### B. Time-Resolved Measurements

While the time-averaged and time-resolved measurements exhibit similar features, the time-resolved IEDFs provide insight into ion energy dynamics and the possible origins of thruster instabilities. Such information is important when choosing an optimum operating condition of an HET, in terms of thruster performance and lifetime. Observing the IEDFs where the primary beam population dominates, at angles with the centerline of less than 45°, shows that the most probable ion energy oscillates at the breathing mode frequency of 27.8 kHz at the 220-W condition or 32.5 kHz for the 330-W condition. This behavior has been heavily documented with other plasma properties such as electron number density, electron temperature, plasma potential, and ion velocity using various time-resolved diagnostics [23–26].

The primary ion beam population exhibits two important behaviors as operating conditions change: the breathing mode frequency and the magnitude of the peak-to-peak ion energy oscillations increase as the discharge voltage is increased. This outcome was expected, as it has been shown that increasing the discharge voltage leads to an increase

in breathing mode oscillation frequency and peak-to-peak discharge voltage oscillations [27–29]. Ion energy is directly linked to the acceleration potential, which is set by the discharge voltage, therefore, any change in temporal characteristics of the discharge voltage will impact time-resolved ion energy. Measuring the behavior of the primary ion beam population is important for determining the impact on the performance, lifetime, stability, and choosing thruster operating points.

As mentioned in Section III a feature only observed at the 330-W condition is a branching structure reaching from primary ion beam energies to elastically scattered energy levels. This feature is believed to be a part of an elastically scattered population as it exists within the expected ion energy range for the given condition, 100 eV – 200 eV. Inspecting Fig. 13, a comparison of the discharge current and time-aligned IEDF is plotted. This elastically scattered population begins when the discharge current or ionization is at its minimum and ends at approximately 25% of the peak discharge current. Interestingly, when comparing the time-resolved IEDFs at the two operating conditions, both possess an elastically scattered population, however, the branching feature is absent at the 220-W condition. The elastically scattered population is present at higher centerline angles at the 220-W condition, but when the centerline angle is decreased below 45° this population has completely disappeared, as compared to the 330-W condition where this population is still partially present. It is possible that as the discharge voltage increases, the ionization and acceleration zones shift upstream towards the anode, resulting in a decrease in plume divergence [28, 30, 31]. Therefore, a reduction in primary beam ions is measured at the 330-W condition for centerline angles above 45°. An additional possibility includes a mode transition from a high amplitude oscillatory mode, similar to the 330-W condition, to a lower amplitude mode as observed in the 220-W condition. This transition may impact the presence of various ion energy populations and lead to the branching feature seen at the 330-W condition [32, 33].

The differences in IEDFs between the two operating conditions highlight how operating parameters influence the ion populations within the plume. As these shifts impact ion behavior at varying angles, the measurement of ion energy populations at high centerline angles, greater than 90°, becomes particularly important, as these charged particles can interact with the spacecraft surfaces, damaging them and interfering with electronics. The highest centerline angle investigated in this study was 82°; however, the RPA used here possessed an acceptance angle of 42° allowing ions beyond 90° to be detected. In this investigation, the ions detected at high centerline angles were primarily composed of CEX ions. The CEX ions measured at these positions were observed to possess energies in the 0 eV – 50 eV range and temporal characteristics that match the main discharge. While this region was shown to be dominated by CEX ions, elastically scattered ions were measured with moderate probabilities, as indicated by Fig. 10a and Fig. 11a.

The various ion energy populations measured during this investigation can be influenced by facility conditions and the environment. Further testing will be conducted at additional vacuum facilities using the same test article, replicating the investigation performed here, allowing the comparison of plume and thruster operation data. Changes in both time-averaged and temporal thruster behavior, as well as plume measurements, are expected. As observed in previous facility effects investigations with HETs, variations in background pressure can affect discharge current, which, as shown here, is linked to ion energy dynamics [34]. The electrical configuration of the facility may also play a role in future experiments, as both electrical boundary conditions and termination pathways have been shown to impact thruster operation [35, 36]. This highlights the importance of accurate characterization of plume behavior in multiple facilities. As a result, the data collected in this investigation will serve as an initial effort in the calibration of PEMs to account for facility effects. By integrating experimental data collected at several facilities to inform upon the impact on thruster plume properties and outputs, improved accuracy of predictions related to thruster performance under different operational conditions may be achieved. The changes in temporal behavior observed with the SPT-50 may inform upon the impact of facility effects on higher power HETs allowing the PEM to be better calibrated.

## VI. Conclusion

An HSRPA was employed to investigate the evolution of ion energy in the plume of the SPT-50 HET, furthering our understanding of the role of ion energy oscillations in HET behavior. Several ion energy populations were measured and observed to oscillate at the breathing mode frequency, including the primary ion beam, elastically scattered ions, and CEX ions. The primary ion beam populations were clearly observed within a centerline angle of 45°, while the elastically scattered and CEX ion populations were found outside of this angle. The temporal features of the primary ion beam population including the magnitude of the peak-to-peak ion energy oscillations and the oscillation frequency both increased with increasing discharge voltage. Several commonalities in time-resolved IEDFs were observed between the two SPT-50 operating conditions tested across the various measurement locations,

including the measurement of ion energy populations with similar features and structures. Additionally, at high centerline angles, a branching effect was observed only at the 330-W condition reaching from primary ion beam energies to elastically scattered energies. The origin of these ions requires further investigation. This investigation has demonstrated the effectiveness of an HSRPA to conduct spatial measurements within the plume of low-power HETs. Lastly, the data collected during this investigation will be utilized to inform upon and calibrate PEMs.

**Acknowledgements**

This work was partially supported by NASA through the Joint Advanced Propulsion Institute, a NASA Space Technology Research Institute, grant number 80NSSC21K1118

## References

[1] S. Weston. "2022 State of the Art Small Spacecraft Technology Report," 2023. [Online]. Available: https://www.nasa.gov/smallsat-institute/sst-soa/2023-report/

[2] R. Wirz, A. Gorodetsky, B. Jorns, & M. Walker. *Predictive Engineering Model for Life and Performance Assessment of High-Power Electric Propulsion Systems*. Presented at the 37th International Electric Propulsion Conference. Massachusetts Institute of Technology, Cambridge, MA USA. 2022.

[3] M. Baird, R. McGee-Sinclair, K. Lemmer, and W. Huang, "Time-resolved ion energy measurements using a retarding potential analyzer," *Review of Scientific Instruments*, vol. 92, no. 7, Jul. 2021, doi: 10.1063/5.0039621.

[4] A. Thomas and K. Lemmer. "Time-resolved Ion Energy Measurements Using a Retarding Potential Analyzer for Electric Propulsion Applications" *Rev. Sci. Inst.,* 1 February 2024; 95 (2): 023505. https://doi.org/10.1063/5.0176167

[5] M. J. Baird, T. V Kerber, K. M. Lemmer, and W. Huang, "Hall Thruster Plume Measurements of Time Resolved Ion Energy." Presented at the 36th International Electric Propulsion Conference, 2019.

[6] D. Manzella, S. Oleson, J. Sankovic, T. Hagg, A. Semenkin, & V. Kim, "Evaluation of Low Power Hall Thruster Propulsion." Presented at the 32nd Joint Propulsion Conference, 1996.

[7] C. Clauss., D. Tilley., & D. Barnhart. *Benefits of Low-Power Stationary Plasma Thruster Propulsion for Small Satellites*. 1995.

[8] C. L. Enloe, High-resolution retarding potential analyzer, *Review of Scientific Instruments*, vol. 65, no. 2, pp. 507–508, 1994, doi: 10.1063/1.1145167.

[9] F. Takens, Detecting strange attractors in turbulence, 1981, pp. 366–381. doi: 10.1007/bfb0091924.

[10] G. Sugihara., R. *May., H. Ye., C. Hsieh., E. Deyle., M. Fogarty., & S. Munch. Detecting Causality in Complex Ecosystems. Science (American Association for the Advancement of Science), 338(6106), 496–500. 2012. https://doi.org/10.1126/science.1227079*

[11] D. Eckhardt, J. Koo, R. Martin, M. Holmes, and K. Hara, Spatiotemporal data fusion and manifold reconstruction in Hall thrusters, *Plasma Sources Sci Technol*, vol. 28, no. 4, Apr. 2019, doi: 10.1088/1361-6595/ab0b1f..

[12] J. P. Sheehan and N. Hershkowitz, Emissive probes. *Plasma Sources Science & Technology*, *20*(6), 063001-1–22. 2011. https://doi.org/10.1088/0963-0252/20/6/063001

[13] J. P. Sheehan, Y. Raitses, N. Hershkowitz, and M. McDonald, Recommended practice for use of emissive probes in electric propulsion testing, 2017, *American Institute of Aeronautics and Astronautics Inc.* doi: 10.2514/1.B35697.

[14] R. F. Kemp and J. M. Sellen, Plasma potential measurements by electron emissive probes,"*Review of Scientific Instruments*, vol. 37, no. 4, pp. 455–461, 1966, doi: 10.1063/1.1720213.

[15] D. M. Goebel and I. Katz, "Fundamentals of Electric Propulsion: Ion and Hall Thrusters. Wiley. 2008

[16] Z. Zhang, Z. Zhang, H. Tang, L. Liang, Y. William, Z. Chen, J. Ren, & J. Cao. Measurement of the distribution of charge exchange ions in a Hall-effect thruster plume, *Plasma Sources Sci Technol*, vol. 29, no. 8, Aug. 2020, doi: 10.1088/1361-6595/aba12c.

[17] J. A. Walker, J. D. Frieman, M. L. R. Walker, V. Khayms, D. King, and P. Y. Peterson, Electrical facility effects on hall-effect-thruster cathode coupling: Discharge oscillations and facility coupling, *J Propuls Power*, vol. 32, no. 4, pp. 844–855, 2016, doi: 10.2514/1.B35835.

[18] J. Sheehan, Y. Raitses, N. Hershkowitz, I. Kaganovich, & N. Fisch. (2011). A comparison of emissive probe techniques for electric potential measurements in a complex plasma. *Physics of Plasmas*, 18(7) https://doi.org/10.1063/1.3601354

[19] K. Dannenmayer, P. Kudrna, M. Tichý, & S. Mazouffre. (2011). Measurement of plasma parameters in the far-field plume of a Hall effect thruster. *Plasma Sources Science and Technology*, 20(6)https://doi.org/10.1088/0963-0252/20/6/065012

[20] V. Kim, V. Kozlov, G. Popov, and A. Skrylnikov, "Plasma Parameter Distribution Determination in SPT -70 Plume. Presented at the 28th International Electric Propulsion Conference, Toulouse, France, 2003

[21] R. Sullivan, P. Torrey, & L. Johnson. *Investigation of High-Energy Ions with High-Angle Trajectories in Hall Thruster Plumes*. Presented at the 30th International Electric Propulsion Conference. 2007.

[22] J. Laube, N. Massaccesi, B. Zitouni, M. Peukert, M. Naeije. EP plasma plume in orbit: Diagnostics and analysis correlation. Presented at the 36th International Electric Propulsion Conference. Vienna, Austria. 2019.

[23] C, Durot, A. Gallimore, & T. Smith. (2014) Validation and evaluation of a novel time-resolved laser-induced fluorescence technique. *Review of Scientific Instruments*, 85(1) https://doi.org/10.1063/1.4856635

[24] V. Chaplin, R. Lobbia, A. Lopez, I. Mikellides, R. Hofer, J. Polk, & A. Friss. (2020). Time-resolved ion velocity measurements in a high-power Hall thruster using laser-induced fluorescence with transfer function averaging. *Applied Physics Letters*, 116(23) https://doi.org/10.1063/5.0007161

[25] R. Lobbia, & A. Gallimore. (2009). *Fusing spatially and temporally separated single-point turbulent plasma flow measurements into two-dimensional time-resolved visualizations*. 12th International Conference on Information Fusion. 2009.
[26] R. Lobbia. "A Time-resolved Investigation of the Hall Thruster Breathing Mode". Ph.D thesis, University of Michigan, (2008).
[27] N. Yamamoto, K. Komurasaki, & Y. Arakawa. (2005). Discharge current oscillation in Hall thrusters. *Journal of Propulsion and Power*, 21(5):870–876. https://doi.org/10.2514/1.12759
[28] M. Baird, T. Kerber, R. McGee-Sinclair, & K. Lemmer. (2021) Plume divergence and discharge oscillations of an accessible low-power hall effect thruster. *Applied Sciences (Switzerland)*, 11(4):1–16. https://doi.org/10.3390/app11041973
[29] G. Xia, X. Liu, H. Li, Y. Ding, L. Wei, S. Chen, & D. Yu. (2020) Performance improvement of Hall thrusters with high discharge voltage. *Vacuum*, 172https://doi.org/10.1016/j.vacuum.2019.109052
[30] Y. Azziz. "Experimental and Theoretical Characterization of a Hall Thruster Plume." Ph.D thesis, Massachusetts Institute of Technology, (2007).
[31] K. Diamant, R. Liang, & R. Corey. (2014). The effect of background pressure on SPT-100 Hall thruster performance. *50th AIAA/ASME/SAE/ASEE Joint Propulsion Conference*, https://doi.org/10.2514/6.2014-3710
[32] M. Sekerak, B. Longmier, A. Gallimore, D. Brown, R. Hofer, & J. Polk. (2013). Mode transitions in hall effect thrusters. *49th AIAA/ASME/SAE/ASEE Joint Propulsion Conference*, 1 PartFhttps://doi.org/10.2514/6.2013-4116
[33] D. Brown & A. Gallimore. *Investigation of Low Discharge Voltage Hall Thruster Operating Modes and Ionization Processes*. Presented at the 31st International Electric Propulsion Conference. University of Michigan, MI, USA. 2009.
[34] W. Huang, H. Kamhawi, & T. Haag. Effect of Background Pressure on the Performance and Plume of the HiVHAc Hall Thruster. Presented at the 33rd International Electric Propulsion Conference. Washington University, Washington, D.C., USA. 2013.
[35] J. Walker, S. Langendorf, M. Walker, V. Khayms, D. King, & P. Perterson. (2016). Electrical facility effects on hall current thrusters: Electron termination pathway manipulation. *Journal of Propulsion and Power*, 32(6):1365–1377. https://doi.org/10.2514/1.B35904
[36] D. Jovel & M. Walker. Current Pathways Model for Hall Thruster Plumes in Ground-based Vacuum Test Facilities: Measurements and Observations. Submitted for publication. (2024).